

# Intrinsic Reduction Kinetics Investigation on a Hematite Oxygen Carrier by CO in Chemical Looping Combustion

Mingze Su,\*<sup>†</sup> Haibo Zhao,<sup>‡</sup> Xin Tian,<sup>‡</sup> Pengfei Zhang,<sup>†</sup> Baozhou Du,<sup>†</sup> and Zhigang Liu\*,<sup>†</sup>

<sup>†</sup>Key Laboratory for Flow & Enhanced Heat Transfer, Energy Research Institute of Shandong Academy of Sciences, Jinan, Shandong 250014, People's Republic of China

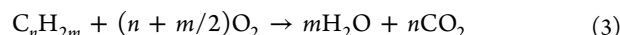
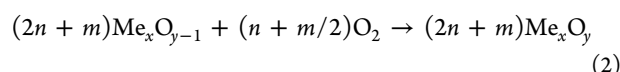
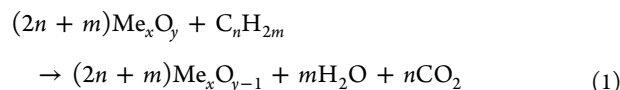
<sup>‡</sup>State Key Laboratory of Coal Combustion, Huazhong University of Science and Technology, Wuhan, Hubei 430074, People's Republic of China

**ABSTRACT:** In the present work, the intrinsic reduction kinetics of a chemical looping oxygen carrier, hematite, reduced by CO has been investigated. Initially, the pore structure features of the hematite OC were tested to provide the necessary parameters for the kinetics analysis. Then, temperature-programmed reduction experiments were conducted in a thermogravimetric analyzer. The results showed that the weight loss rate appears to be a bimodal distribution and the appropriate experimental temperature range for the intrinsic kinetics testing of the first reduction stage of hematite is 400–650 °C. Additionally, a series of experiments were further conducted in a batch fluidized bed system with different temperatures and different CO concentrations. After elimination of the internal and external diffusion limitations, the intrinsic activation energy and pre-exponential factor were determined as 74.48 kJ/mol and  $1.2 \times 10^{12} \text{ s}^{-1}$ , respectively. The analysis of the internal and external diffusion effects was beneficial to understand the reaction characteristics of this kind of hematite oxygen carrier. As concluded, the shrinking core series model, the external diffusion control, and the small apparent activation energy obtained from many previous studies were compatible with this analysis and can be explained by this work. The research results attained in this study can also contribute to the development of a practical model for computational fluid dynamics simulation.

## 1. INTRODUCTION

Chemical looping combustion (CLC), which has the characteristic of  $\text{CO}_2$  inherent separation, has been considered as a very promising fossil fuel utilization technology for addressing the global warming issue.<sup>1,2</sup> Because CLC splits the conventional combustion process into two separate redox processes, the gas composition separation ( $\text{CO}_2$  separation from flue gas) in conventional  $\text{CO}_2$  capture techniques can be substituted by the gas–solid [flue gas–oxygen carrier (OC) particles] separations in CLC. In such a way, much higher energy conversion efficiency can be achieved as well as much lower cost for  $\text{CO}_2$  capture.<sup>3,4</sup> Basically, lattice oxygen is cyclically transferred to oxidize the fuel with the aid of the OC circulation in CLC. In general, the CLC reactor is composed of an air reactor (AR) and a fuel reactor (FR). Air and fuel enter the AR and FR separately and without direct contact. The schematic view of the CLC reactor is shown in Figure 1. The fossil fuel is oxidized via OCs with high oxygen potential (usually metal oxide,

$\text{Me}_x\text{O}_y$ ) in FR and comes out as  $\text{CO}_2$ ,  $\text{H}_2\text{O}$ , and OCs with low oxygen potential ( $\text{Me}_x\text{O}_{y-1}$ ) (see eq 1). High-purity  $\text{CO}_2$  can be easily obtained by a simple condensation treatment to the flue gas of the FR.



$\text{Me}_x\text{O}_y$  can be regenerated in AR (see eq 2). In this way, a loop can be formed as produced  $\text{Me}_x\text{O}_y$  is further transferred back to the FR. The overall reaction of the traditional combustion process (see eq 3) is the sum of eqs 1 and 2 indeed.

$\text{Fe}_2\text{O}_3$  is regarded as a kind of cheap and environmentally friendly OC material. Among all of the Fe-based OCs, iron ore has been widely adopted as OC in most pilot-scale CLC systems. The reaction mechanism and kinetics of Fe-based OCs have already been reported in some literature. Elgeassy et al.<sup>5</sup> and Ettabirou et al.<sup>6</sup> have studied the reduction kinetics of  $\text{Fe}_2\text{O}_3$  by CO decades ago. However, the obtained kinetics, which was only limited to the metallurgical industry, might not be applicable to the CLC processes. On the basis of thermodynamic analysis, Wang et al.<sup>7</sup> pointed out that the

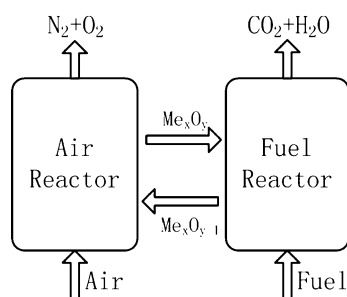


Figure 1. Schematic view of the CLC reactor.

Received: October 28, 2016

Revised: February 11, 2017

Published: February 13, 2017

active material,  $\text{Fe}_2\text{O}_3$ , would react with the inert support,  $\text{Al}_2\text{O}_3$ , to produce  $\text{FeAl}_2\text{O}_4$ , which plays a negative role in the reactivity of the OC. Zafar et al.<sup>8</sup> found that  $\text{Fe}_2\text{O}_3$ -based OC demonstrates high reactivity in the first reduction stage ( $\text{Fe}_2\text{O}_3$  to  $\text{Fe}_3\text{O}_4$ ) but typical low reactivity was observed in the second reduction stage ( $\text{Fe}_3\text{O}_4$  to  $\text{FeO}$ ). Abad et al.<sup>9,10</sup> examined the apparent kinetics of the synthetic Cu-, Fe-, and Ni-based OCs reduced by CO,  $\text{H}_2$ , and  $\text{CH}_4$ , for the purpose of providing key kinetic parameters for reactor design and computational fluid dynamics (CFD) simulation. Obviously, the obtained small activation energy indicates that the diffusion effect had not been fully eliminated in their experiments. Chen et al.<sup>11</sup> investigated the reduction kinetics of hematite in a micro-fluidized bed reactor. Unfortunately, the effect of the reducing gas concentration was not discussed in their study.

The heterogeneous gas–solid reaction is regarded as one of the most complex processes in nature. The overall reaction includes both the chemical reaction process and the mass/heat transfer processes; moreover, the solid material/surface is also difficult to be characterized. The intrinsic reaction kinetics and the internal/external mass transfer effects should be comprehensively considered when a kinetic equation is established. As reviewed in the literature, there is no agreement on the rate-controlling step for the reduction of OC, let alone the reported rate constant and activation energy. Monazam et al.<sup>12</sup> claimed that the overall reduction process of  $\text{Fe}_2\text{O}_3$  to  $\text{FeO}$  consists of two parallel reduction reactions, i.e.,  $\text{Fe}_2\text{O}_3$  to  $\text{Fe}_3\text{O}_4$  and  $\text{Fe}_3\text{O}_4$  to  $\text{FeO}$ . Experiments were conducted for fitting the new kinetic model proposed, with temperatures ranged from 973 to 1098 K and  $\text{CH}_4$  concentrations of 15–35 vol %. Abad et al.<sup>13</sup> adopted the shrinking core model to describe the reduction process of  $\text{Fe}_2\text{O}_3$  with syngas. Go et al.<sup>14</sup> concluded that, in the temperature range for CLC operation (1073–1173 K), the reduction of iron oxide by  $\text{CH}_4$  was controlled by the external gas diffusion. Piotrowski et al.<sup>15,16</sup> obtained the apparent activation energy for reactions of  $\text{Fe}_2\text{O}_3$  with CO and  $\text{H}_2$  within a wide range of 25–125 kJ/mol. They concluded that the two-dimensional (2D) nucleation growth model is suitable to describe the reaction process. Pineau et al.<sup>17</sup> conducted a series of low-temperature (as low as 493 K) experiments to investigate the reduction kinetics of hematite being reduced by  $\text{H}_2$ . Two different reduction stages were distinguished during the overall reduction process, and the activation energy was determined as 76 kJ/mol for the first reduction stage and 39 kJ/mol for the second reduction stage. They also pointed out that the overall reaction is the phase boundary reaction controlled at higher temperatures. Because most of CLC reactors using hematite as the OC were designed for only using the first reduction stage, in our previous work,<sup>18</sup> we pointed out that the first reduction stage of hematite OC was controlled by external gas diffusion when the operation temperature reaches 900 °C in thermogravimetric analyzer (TGA) and the apparent activation energy is meaningless in this condition. Chuang et al.<sup>19</sup> conducted experiments in a fluidized bed reactor to investigate the intrinsic reduction kinetics of the Cu-based OC. By elimination of the internal and external diffusion effects, they pointed out that measurements of the intrinsic kinetics could only be achieved at small particle size and low temperature. They concluded that the intrinsic activation energy for the reaction of  $\text{Cu}_2\text{O}$  reduced by CO is 49 kJ/mol.

To illustrate the reaction mechanism of Fe-based OC reduced by CO at a microcosmic level, Dong et al.<sup>20–25</sup> carried out a series of density functional theory (DFT) simulations.

First, the reduction activities of the surfaces (1102) and (0001) of  $\text{Fe}_2\text{O}_3$  were studied, and the best adsorption sites were identified.<sup>20</sup> As concluded, the surface (1102) is more prone to reacting with CO than the surface (0001). Then, a possible reaction mechanism for the reduction of Fe-based OC by CO was proposed:<sup>21</sup>  $\text{Fe}_2\text{O}_3$  will be activated by one CO molecule to produce  $\text{Fe}_2\text{O}_2\text{O}$ , and then the activated O molecule will be reduced by another CO molecule to produce  $\text{CO}_2$ . After that, they pointed out that the energy barrier of the second reduction stage is far larger than that of the first stage;<sup>22</sup> thus, it is inadvisable to reduce the  $\text{Fe}_2\text{O}_3$ -based OC deeply in practical CLC application. Finally, they examined the effect of the inert carriers, such as  $\text{ZrO}_2$ ,  $\text{MgO}$ , and  $\text{Al}_2\text{O}_3$ , on the reactivity of  $\text{Fe}_2\text{O}_3$  with CO.<sup>23–25</sup> They concluded that the inert carriers promote the adsorption of CO on  $\text{Fe}_2\text{O}_3$  and the electron transfer from the inert carriers to  $\text{Fe}_2\text{O}_3$  lengthens the Fe–O bond, which is beneficial to the reduction of  $\text{Fe}_2\text{O}_3$ . The energy barriers of the reactions were determined as 2.59, 0.99, 0.98, and 0.83 eV for the reduction of  $\text{Fe}_2\text{O}_3$ ,  $\text{Fe}_2\text{O}_3/\text{Al}_2\text{O}_3$ ,  $\text{Fe}_2\text{O}_3/\text{MgO}$ , and  $\text{Fe}_2\text{O}_3/\text{ZrO}_2$ , respectively.

Although the reduction of hematite OC has been widely studied, its reduction kinetics is still unclear (especially for the first reduction stage) and there exists a huge gap between experimental measurements and quantum chemistry calculations. In this work, the intrinsic kinetics of a kind of hematite OC reduced by CO was experimentally investigated. Initially, the Brunauer–Emmett–Teller (BET) surface area test was conducted to provide necessary parameters for theoretical analysis. Then, temperature-programmed reduction experiments were conducted in TGA to determine an appropriate temperature range for the intrinsic kinetics testing. Finally, a series of formal experiments were conducted in a batch fluidized bed reactor with different temperatures and different CO concentrations to analyze the intrinsic kinetics, and the effects of the internal and external diffusion factors were also discussed.

## 2. EXPERIMENTAL SECTION

The iron ore originated from the E'kou mine, China. The physical and chemical properties of this hematite OC can be considered to be stable in this study. Factually, the OC tested in this work has been previously used for more than 300 h in a 5 kW<sub>th</sub> interconnected fluidized bed reactor.<sup>26,27</sup> The OC has been fully oxidized before tests, and the elemental analysis [as determined by X-ray fluorescence (XRF, EDAX EAGLE III)] showed that the mass fraction of  $\text{Fe}_2\text{O}_3$  is 66 wt %.<sup>28</sup> The particles in the diameter range of 180–200  $\mu\text{m}$  by sieving were collected as the samples in this experiment. The granule density of the particles is 3472 kg/m<sup>3</sup>. Characterizations of this material, such as X-ray diffraction (XRD, EM-PYREAN) analysis and BET surface area (JW-BK132F) analysis, will be shown in the following section.

Under the heating rate of 15 °C/min and 15 and 50 vol % CO balanced by  $\text{N}_2$  as the reducing gas, temperature-programmed reduction experiments were conducted in TGA (Netzsch STA409PC). The sample mass was 12.5 mg, and the final temperature for both tests was 970 °C. The weight loss peaks will be discussed later.

After that, experiments were further conducted in a batch fluidized bed reactor to investigate the intrinsic reduction kinetics of the first reduction stage of hematite OC. A total of 5 g of hematite was chosen as the active OC, and 15 g of silica sand was chosen as the inert bed material. The main reason for adding silica sand is to reduce the error coming from the sample loss. Reducing gas of 5, 7.5, and 15 vol % CO balanced by  $\text{N}_2$  was introduced into the reactor with a flow rate of 1 L/min in the reduction period. The experiments were conducted at 400, 425, 450, 475, 555, 600, and 647 °C, separately. The choice of these

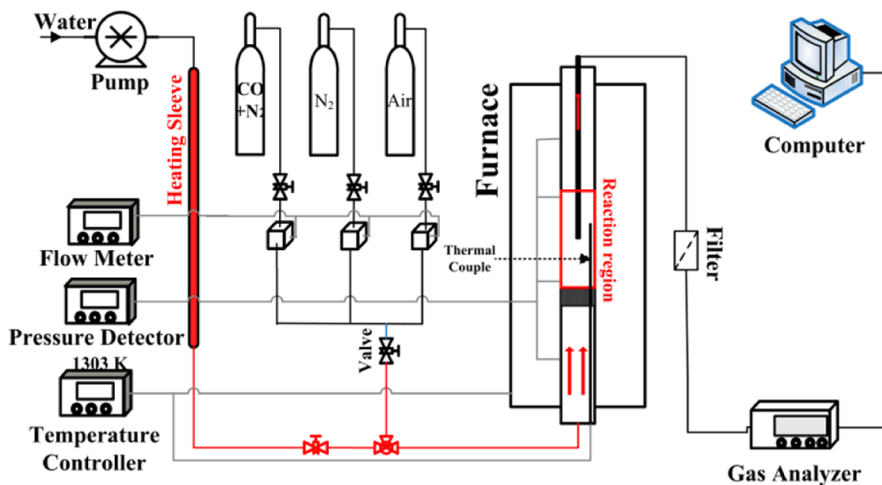


**Figure 2.** Schematic view of the fluidized bed reactor.

temperatures depends upon the analysis of the TGA results. The schematic view of the fluidized bed experimental rig is presented in Figure 2. The diameter of the reaction chamber is 33 mm, and the exhaust gas was detected by the online gas analyzer (Gasboard 3100P, Cubic Optoelectronics).

For the batch fluidized bed experiment, we considered  $\text{N}_2$  as the characteristic fluidization agent. The lowest operation temperature, 400 °C (where the worst fluidization occurs), was considered as the reference temperature for analysis. The density and viscosity of  $\text{N}_2$  at 400 °C are 0.552 kg/m<sup>3</sup> and  $3.18 \times 10^{-5}$  Pa s, respectively. The Archimedes number,  $Ar = (d_p^3 \rho_f (\rho_p - \rho_f) g) / (\mu_f^2)$ , is 127.37. Then, the critical Reynolds number, which can be calculated from the correlation of Wen and Yu,<sup>29</sup>  $Re_{p,mf} = (33.7^2 + 0.0408Ar)^{0.5} - 33.7$ , is 0.077. The superficial velocity at incipient fluidization,  $U_{mf}$ , is equal to 0.0233 m/s. Under the operation condition, the superficial velocity,  $U$ , equals 0.0442 m/s, which gives  $U/U_{mf} = 1.89$ . As seen, the bed material was always fluidized in our experiments.

### 3. RESULTS

**3.1. BET Surface Area and Pore Size Distribution.** The pore size distribution of the OC particle after redox cycles is shown in Figure 3. The most probable pore radius and the mean pore radius ( $\bar{r}_p$ ) are 3.051 and 12.904 nm, respectively. The BET surface area,  $S'_{\text{BET}}$ , is 1.387 m<sup>2</sup>/g. Thus, the porosity of this material,  $\varepsilon = \bar{r}_p S'_{\text{BET}} / 2$ , is 0.031. The surface area per volume of the solid material,  $S'_{\text{BET}}$ , was attained according to the

particle density.  $S'_{\text{BET}} = 4.86 \times 10^6 \text{ m}^2/\text{m}^3$ . In this sense, this hematite OC is nearly compact and relatively impermeable. This can also be verified by the SEM microphotographs of this material.<sup>26</sup> As a result, it can be imagined that the reducing gas can hardly permeate deeply into the interior of the particles under the reaction environment.

Breault et al.<sup>30</sup> pointed out that the surface area was highly dependent upon the temperature. On one hand, the grain structure changes with the temperature. To be more specific, the grain size, porosity, and diameter of the pore become larger, while the specific surface area becomes smaller, as the grain agglomerates at high temperatures. On the other hand, the grain structure changes with the material property. This is to say, the reactant and product with different material properties, especially the molar volume, will influence the grain structure during the reaction process. As stated in section 2, the hematite OC tested in the present work has been previously used for more than 300 h in the 5 kW<sub>th</sub> CLC reactor. The previous experiments can be regarded as the pretreatment process to the hematite OC, and it is believed that the pore structure of the OC is stable in the present experiment. Therefore, the agglomeration effect could be neglected. In addition, the analyses in the present work were based on the reaction rates at the beginning of the reactions, and there is almost no  $\text{Fe}_3\text{O}_4$  generated at this point. That is to say, the effects of material change could also be neglected.

**3.2. Temperature-Programmed Reduction Experiments.** The derivative thermogravimetry (DTG) curves obtained in temperature-programmed reduction experiments are shown in Figure 4. It can be seen that both DTG curves appear to be bimodal distribution, which illustrates that the reduction reaction of the hematite OC happens stage by stage indeed. The peak position changes as the volume fraction of CO. To be more specific, the maximum weight loss rates appear at 429.8 and 711.3 °C under a 50 vol % CO environment, while they change to 533.3 and 874.1 °C under a 15 vol % CO environment. Although the temperature points with the maximum weight loss rates may change with different reducing gas concentrations, the first reduction stage always happens under the temperature range of 400–600 °C. The first reduction reaction terminates after 600 °C, because the  $\text{Fe}_2\text{O}_3$  component has converted to  $\text{Fe}_3\text{O}_4$  completely before 600 °C. In a real CLC process, the OC usually circulates under relatively high temperatures and the OC particles introduced

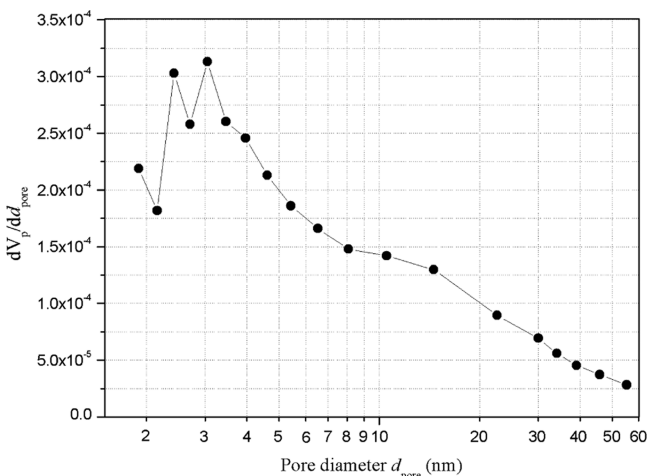


**Figure 3.** Pore size distribution of the hematite OC.

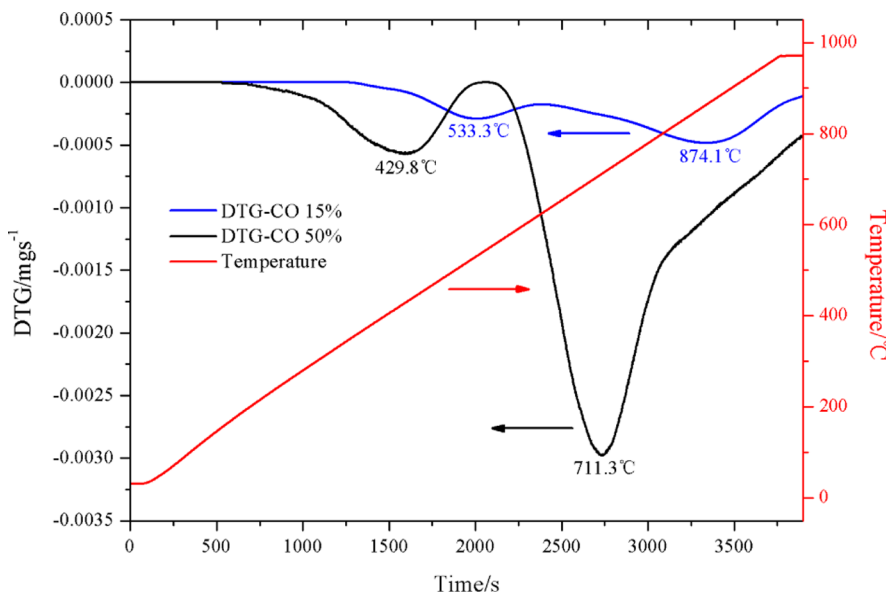


**Figure 4.** DTG results for the temperature-programmed reduction experiments.

into the fuel reactor will be heated rapidly; thus, the first reduction stage can only happen under high-temperature conditions. Because the first reduction stage could happen at a typical low temperature, the reaction under high temperatures may be controlled by external mass transfer. This is also consistent with conclusions obtained from our previous research.<sup>18</sup>

In the batch fluidized bed experiments, CO was consumed when it flowed through the bed materials, which results in the fact that the outlet CO concentration is smaller than that of the inlet. Therefore, the CO concentration adopted in data processing is an important issue that should be appropriately addressed. Although most researchers (including us) take the logarithmic average (see section 3.3.1) as the characteristic value, this treatment may also introduce some errors to the kinetics analysis. For a better accuracy, consumed CO should be restricted to a relatively small amount; thus, a low reaction rate is required. Another aim of the TGA experiments is to seek the appropriate temperature range for the batch fluidized bed experiments. As mentioned above, the intrinsic reduction kinetics of the first reduction stage of hematite should not be tested under the temperature condition of a real CLC process, i.e., 900 °C or higher, and should be tested within the temperature range of 400 to 600 °C, because the intrinsic kinetics will be distorted as a result of the limitation of gas diffusion at higher temperatures. On the basis of this understanding, 400–650 °C was chosen as the temperature window for the batch fluidized bed experiments later. Lower temperatures are also beneficial to determine the CO volume fraction more accurately.

**3.3. Batch Fluidized Bed Experiment.** **3.3.1. Data Processing Method.** The flow rate and volume fraction of the exhaust gas components were detected online in the batch fluidized bed experiments. Because no CO<sub>2</sub> was detected during the OC oxidation period, it can be considered that no carbon deposition (no coking) occurred during the reduction period. The conversion ( $X$ ) as a function of time can be calculated as

$$X = \frac{\int_{t_0}^t F_{\text{ex}} Y_{\text{CO}_2} dt}{\int_{t_0}^{t_{\text{total}}} F_{\text{ex}} Y_{\text{CO}_2} dt} \quad (4)$$

where  $F_{\text{ex}}$  is the flow rate of the exhaust gas and  $Y_{\text{CO}_2}$  represents the volume fraction of CO<sub>2</sub> in the product gas.

A typical profile for the product gas concentration detected by the gas analyzer is also shown in Figure 5. CO is considered

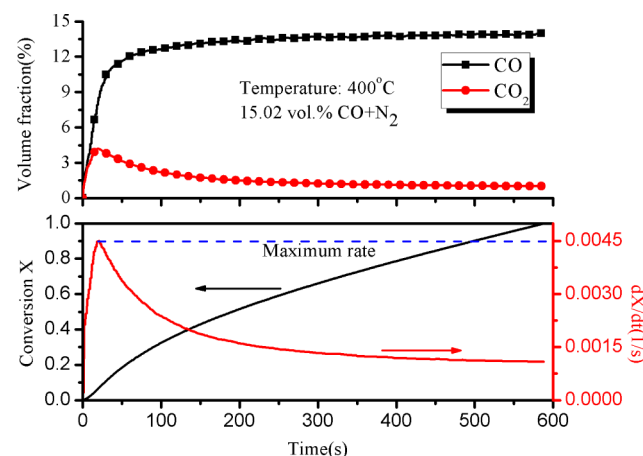


**Figure 5.** Typical profile of the exhaust gas concentration and the calculated conversion rate.

as excessive for the intrinsic kinetics testing, without the influence of the aeration rate. As mentioned above, the logarithmic-averaged volume fraction was introduced as the characteristic CO volume fraction. The logarithmic average can be calculated as

$$Y_{\text{ave}} = \frac{Y_{\text{in}} - Y_{\text{out}}}{\ln(Y_{\text{in}}/Y_{\text{out}})} \quad (5)$$

where  $Y_{\text{in}}$  and  $Y_{\text{out}}$  represent the inlet and outlet volume fractions for the same gas component, respectively. The logarithmic-averaged volume fraction will be used in the formal

Arrhenius plotting (e.g., Figure 7), while the inlet volume fraction (as a simplification) will be used in the direct Arrhenius plotting (e.g., Figures 8 and 9). Without this simplification, the direct Arrhenius plotting would be impossible to obtain, because the points in the same group do not have the same logarithmic-averaged volume fraction.

The profile of the conversion and conversion rate as a function of time obtained in the typical test is also shown in Figure 5. The conversion rate appears at a maximum value at the beginning of the reaction. Before the maximum value is reached, there exists a rising process, which may result from the combination effect of gas mixing in the reactor and gas diffusion to the particle surface. The maximum reaction rate can be regarded as the reaction rate when the solid conversion,  $X$ , was equal to 0. Therefore, the maximum values were chosen as the characteristic reaction rates for analysis. The Arrhenius-type apparent kinetics equation can be used to describe the conversion profile as follows:

$$\frac{dX}{dt} = k' \exp(-E/RT)f(X)g(Y_{CO}) \quad (6)$$

where  $X$  represents the conversion of OC,  $k'$  is the pre-exponential factor,  $E$  is the apparent activation energy,  $R$  represents the universal gas constant,  $T$  is the reaction temperature, and  $Y_{CO}$  represents the mole/volume fraction of the reducing gas.  $f(X)$  is the reaction mechanism function in differential form, which reflects the functional relationship between the reaction rate,  $dX/dt$ , and the solid conversion,  $X$ . According to the scale investigated,  $f(X)$  can be grouped into two categories: the particle function and the grain function. Within the particle function, the homogeneous reaction model is usually represented as  $f(X) = 1 - X$ , while the shrinking core model is usually represented as  $f(X) = (1 - X)^{2/3}$ . Generally speaking, the homogeneous reaction model corresponds to the situation that the overall reaction is not affected by the internal diffusion, while the shrinking core model is satisfying when the overall reaction is highly affected by the internal diffusion.  $g(Y_{CO})$  represents the relationship between the reaction rate with the reducing gas concentration. The simplest form,  $g(Y_{CO}) = Y_{CO}^n$ , was applied in this study, although several researchers (e.g., Monson et al.<sup>31</sup>) have reported that the power function correlation does not apply well over a wide range of gas concentrations.

**3.3.2. Effect of the External Diffusion.** To evaluate the effect of external diffusion, the reaction rate measured in the experiment was compared to the maximum rate that could be reached under the gas diffusion control, as shown in Figure 6. The mass transfer rate,  $r_{ext}$  ( $\text{mol g}^{-1} \text{s}^{-1}$ ), can be calculated as

$$r_{ext} = k_g S_m (C_B - C_s) \quad (7)$$

where  $C_B$  represents the bulk concentration of CO (i.e., 2.76  $\text{mol/m}^3$  under the condition of 450 °C and volume fraction of 15 vol % CO) and  $C_s$  is the concentration of CO on the external surface of a particle. To calculate the maximum reaction rate,  $C_s$  is assumed to be 0.  $S_m = 0.0091 \text{ m}^2/\text{g}$  is the nominal external surface area per unit mass (g) of the OC particle (here, the particles were considered to be absolutely spherical).  $k_g$  is the external mass transfer coefficient and can be calculated according to the mass transfer correlation.<sup>32</sup>

$$Sh = 2\epsilon_s + 0.69Re_p^{1/2}Sc^{1/3} \quad (8)$$

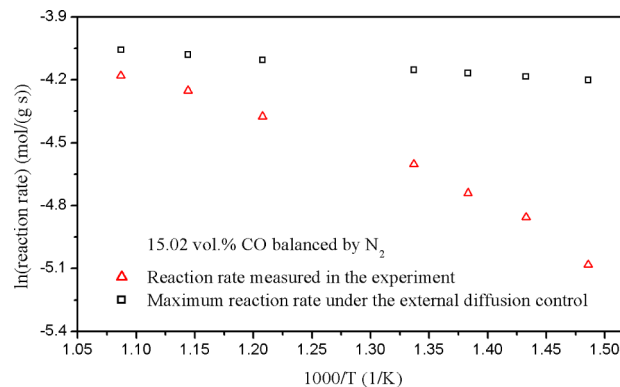


**Figure 6.** Comparison between the maximum rate reached under the diffusion-controlled regime and the measured reaction rate.

The Sherwood number,  $Sh$ , is defined as  $Sh = k_g d_p / D_G$ . Here,  $d_p$  is the diameter of the OC particle (0.19 mm),  $D_G$  is the molecular diffusivity for CO and N<sub>2</sub> (i.e.,  $5.49 \times 10^{-5} \text{ m}^2/\text{s}$  under the condition of 450 °C),  $\epsilon_s$  is the voidage of the fluidized bed material (i.e., 0.926; silica sand was taken as voidage), and the Reynolds number,  $Re_p$ , can be calculated as  $Re_p = Ud_p / \epsilon_s \nu$ .  $U$  represents the superficial gas velocity (i.e.,  $4.73 \times 10^{-2} \text{ m/s}$  under the condition of 450 °C), and  $\nu$  represents the kinematic viscosity of the gas mixing (i.e.,  $6.48 \times 10^{-5} \text{ m}^2/\text{s}$  at 450 °C). The Schmidt number  $Sc = \nu / D_G$ . Breault et al.<sup>33</sup> pointed out that the only way that the researcher can accurately account for external mass transfer is to make measurements in their systems. However, it seems that it is unpractical, especially at high-temperature conditions, such as the CLC processes. In fact, the correlation used in this study has been widely adopted by many researchers.<sup>34,35</sup>

It is clear that, under a lower temperature condition, greater difference exists between calculated and measured rates. Obviously, the measured rates were always smaller than the maximum rate that can be reached under the diffusion-controlled regime. In conclusion, it could be considered that the overall reduction reaction of the hematite OC was not affected by the external gas diffusion when the reaction temperature was lower than 500 °C in these batch fluidized bed experiments. However, under the reaction condition of a real CLC process, i.e., at 900 °C or even higher, the overall reaction of the first reduction stage could be fully controlled by the external gas diffusion.

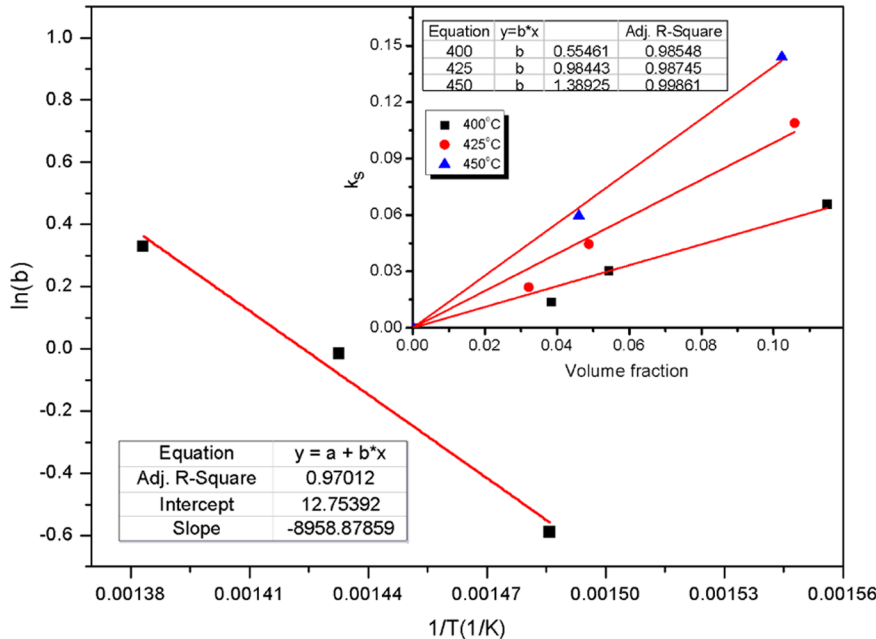
**3.3.3. Effect of the Internal Diffusion and the Intrinsic Kinetics.** As concluded in section 3.3.2, the external diffusion has little influence on the overall reaction rate under the lower temperature conditions. Thus, the effect of the external diffusion will be neglected in the later analysis. That is to say, the concentration of CO on the external surface of the particle is equal to the bulk concentration. Obviously, this simplification is not accurate at higher temperature conditions; thus, the intrinsic kinetics were only obtained through fitting the experimental results obtained under lower temperature conditions. Nevertheless, as reference, the effectiveness factor for the internal diffusion,  $\eta$ , was also calculated for higher temperature conditions. At this point, the overall reaction rate,  $k_{overall}$ , can be expressed as

$$k_{overall} = \eta k_s \quad (9)$$

where  $k_s$  is the intrinsic reaction rate, and  $\eta$  represents the ratio of the reaction rate with diffusion resistance to that without

**Table 1.** Relationships of  $\eta$  and  $k_s$  with the Experimental Temperatures (15 vol % CO)

temperature (°C)	400	425	450	475	555	600	647
$\eta$	0.00477	0.00375	0.00330	0.00283	0.00217	0.00188	0.00171
$k_s$	0.0659	0.1088	0.1441	0.1991	0.3616	0.4991	0.6192

**Figure 7.** Arrhenius plot for  $k_s$ .

diffusion resistance.  $\eta \rightarrow 1$  means that the heterogeneous reaction rate is relatively lower when compared to the gas diffusion in the pore. Hence, the concentration of the reducing gas in the pore was equal to that on the external surface of the particle. In this case, the heterogeneous reaction happens on the whole surface of the particle, and the mechanism function may show as a homogeneous function. On the other side,  $\eta \rightarrow 0$  represents that the heterogeneous reaction happens only on the external layer of the particle, because the reducing gas will be consumed before diffusing into the interior of the particle through the pore. In this case, the mechanism function of the overall reaction may correspond to the shrinking core model.

$\eta$  can be calculated by iterating eq 9 and the following two equations:<sup>36</sup>

$$\eta = (1/3\Phi^2)(3\Phi \coth 3\Phi - 1) \quad (10)$$

$$\Phi = (d_p/6)\sqrt{k_s m_v / D_{\text{eff}}} \quad (11)$$

where  $\Phi$  is the Thiele modulus,  $m_v$  represents the solid mass per unit volume of carrier ( $3.47 \times 10^6$  g/m<sup>3</sup>),  $D_{\text{eff}}$  is the effective diffusivity of CO within the pore, which can be calculated as  $D_{\text{eff}} = \epsilon^2/(1/D_K + 1/D_G)$ <sup>37</sup> (i.e.,  $5.46 \times 10^{-9}$  m<sup>2</sup>/s under the condition of 450 °C),  $D_K$  is the Knudsen diffusivity (i.e.,  $6.34 \times 10^{-6}$  m<sup>2</sup>/s at 450 °C), and  $\epsilon = 0.031$  is the porosity of the OC particle, which has been gained in section 3.1. The calculated effectiveness factors when using 15 vol % CO as the reducing gas are shown in Table 1.

From Table 1, it can be seen that the effectiveness factors are far smaller than 1 for all tests, which illustrates that the gas–solid reaction happens on the external layer of the particles and the overall reactions can be described by the shrinking core model. On the other hand, the effectiveness factors decrease as

the temperature increases, indicating that the reaction layer becomes thinner with the increase of the temperature. The gas–solid contact surface for the heterogeneous reaction becomes smaller under a higher temperature condition than that under a lower temperature condition. This change partially offsets the reactivity-induced improvement of the overall reaction rate, which results in a much lower value of the activation energy. The intrinsic reaction rate,  $k_s$ , which can be obtained in the above analysis simultaneously, is also shown in Table 1.

The tests with the same reaction temperature are taken as a group.  $k_s$  as a function of the CO volume fraction at different temperatures is shown in Figure 7. It can be seen that the intrinsic reaction rates have good linearity with the volume fraction of the reducing gas; thus, the reaction order,  $n$ , can be concluded as 1. Different constants,  $b$ , were obtained for different temperatures. Arrhenius analysis [ $\ln(b)$  as a function of  $1/T$ , also shown in Figure 7] gave an activation energy of 74.48 kJ/mol and a pre-exponential factor of  $3.46 \times 10^6$ . Considering the relationship between  $k_s$  and  $k_v$ , i.e.,  $k_v = k_s m_v$ , the final version of the reaction rate equation can be expressed as

$$k_v = 1.2 \times 10^{12} \exp\left(\frac{-74480}{RT}\right) Y_{\text{CO}} \quad (12)$$

The activation energy of 74.48 kJ/mol corresponds to the energy barrier of 0.774 eV in the DFT simulation, which is almost consistent with the previous simulation results.<sup>23–25</sup> Interestingly, the pre-exponential factor of  $1.2 \times 10^{12}$  s<sup>-1</sup> was close to the theoretical value of the vibrational frequency of the atom in the potential minimum at a low temperature ( $k_B T/h =$

$1.5 \times 10^{13} \text{ s}^{-1}$ , where the Planck constant  $h = 6.626 \times 10^{-34} \text{ J s}$  and the Boltzmann constant  $k_B = 1.381 \times 10^{-23} \text{ J/K}$ .

For validation, as described in section 3.3.1, the results with the same inlet concentration were analyzed in a group. The results of the Arrhenius analysis [ $\ln(k_s)$  as a function of  $1/T$ ] for each group is shown in Figure 8. The activation energies

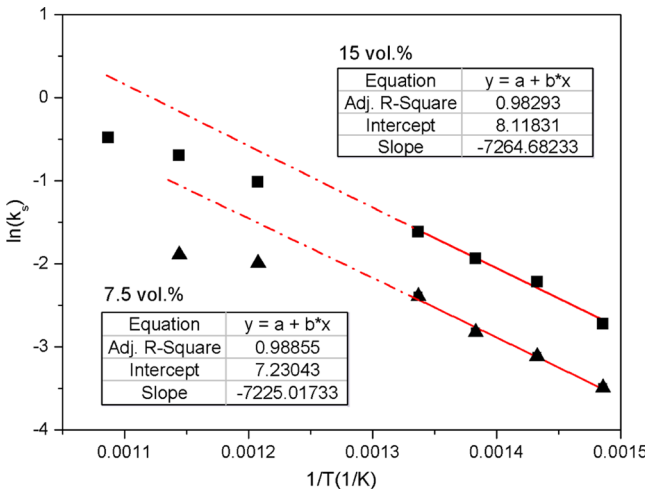


Figure 8. Direct Arrhenius plot for  $k_s$ .

were determined as 60.40 and 60.07 kJ/mol, respectively, which are smaller than the activation energy obtained above (74.48 kJ/mol). It is because, although the inlet CO concentrations have the same value for the same group, the characteristic concentrations are not equal for each point in the same group because the outlet concentrations are different. Grouping experimental results according to the inlet concentration will bring errors to the analysis. From Figure 8, it can also be seen that the results at a higher temperature deviate from the extrapolation of the low-temperature experimental results. It is because the high-temperature reduction reaction is influenced by the external mass transfer.

Many researchers obtained relatively low activation energies in their studies, even as small as 19 kJ/mol.<sup>38</sup> If fitting the apparent reaction rate,  $k_{\text{overall}}$ , directly, as shown in Figure 9, a lower activation energy result (about 31.94 kJ/mol) can also be obtained in our study. From this perspective, the internal

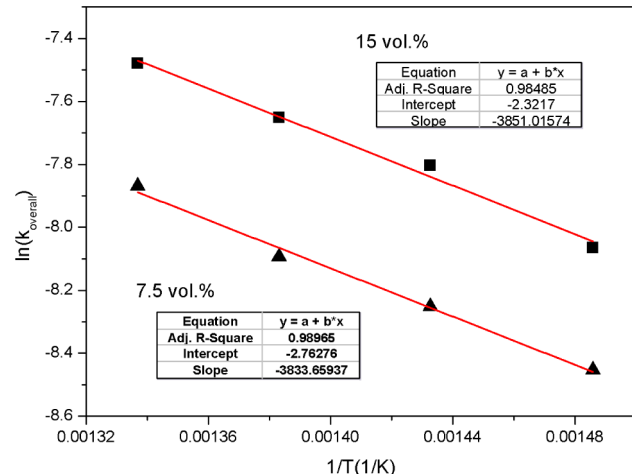


Figure 9. Direct Arrhenius plot for  $k_{\text{overall}}$ .

diffusion effect should be carefully treated for pursuing the intrinsic reaction kinetics of the OC reduction.

XRD analysis was conducted for the samples in the oxidation and reduction states, respectively. As shown in Figure 10,  $\text{SiO}_2$

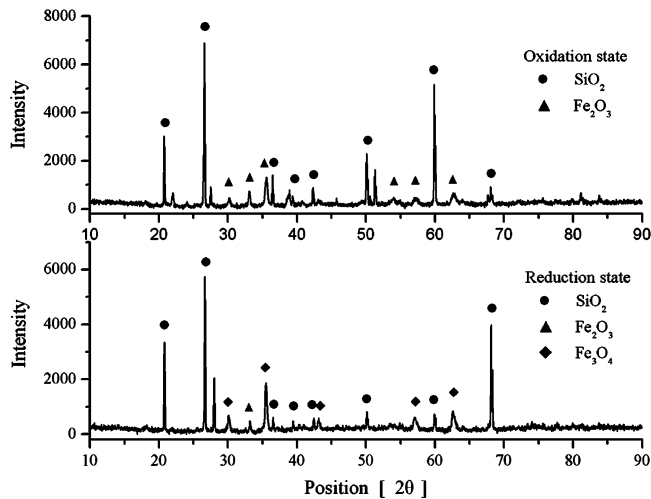


Figure 10. XRD patterns of the samples in the oxidation and reduction states.

composition was detected for both samples, which is because, in the batch fluidized bed experiments, silica sand was used as the main bed material. The samples at different states in XRD analysis both gained from the used bed materials, and the silica sand cannot be removed thoroughly.  $\text{Fe}_2\text{O}_3$  and  $\text{Fe}_3\text{O}_4$  were the main compositions for the samples in the oxidation and reduction states, respectively, which illustrates that the intrinsic kinetics obtained in the above experiments corresponds to the first reduction stage of the hematite OC indeed.

#### 4. DISCUSSION

Obviously, the above analysis and results were compatible with previous conclusions, and this analysis can provide a systematical explanation for the previous conclusions. It can be seen that this hematite OC is nearly compact and relatively impermeable, which results in the fact that reducing gas can hardly permeate into the particles deeply, even under a low-temperature condition. Under higher temperature conditions, the overall reaction rate is limited by the external gas diffusion (see section 3.3.2); therefore, the concentration of the reducing gas around the external surface of particle is nearly equal to zero, making the reducing gas more difficult to permeate into the particles. The above two factors support the shrinking core series model (particle is reduced layer by layer from outside to inside). It should be noted that, although the shrinking core series model was supported by the analyses, that is not to say that the relationship between the reaction rate and the solid conversion is  $dX/dt \sim (1-X)^{2/3}$  definitely, because the solid conversion process may also be affected by the ash content in the condition of  $X \neq 0$ . The actual relationship should depend upon experiments in which the complete conversion process is conducted under the characteristic reaction conditions.

The above results show that the intrinsic activation energy is 74.48 kJ/mol, which is larger than some results of other researchers.<sup>10,38</sup> Low intrinsic activation energy (e.g., 19 kJ/mol<sup>38</sup>) is unconvincing, because a reaction system with such a small activation energy may be unstable at room temperature.

In fact, the value of 19 kJ/mol was even close to the energy barrier of chemisorption. Although the DFT calculation has its limitation, all simulation results reported<sup>23–25</sup> do not support the low activation energy, while some results agree well with the activation energy that we obtained.

There are three reasons to explain why many researchers get low activation energies using different analysis techniques. First, the experimental results were influenced more or less by the external mass transfer, because the experimental conditions were not so reasonable. As shown in this study, the external mass transfer factor will become remarkable under a high-temperature condition. It is well-known that the apparent activation energy was usually smaller than 20 kJ/mol when the reaction rate was controlled by the external mass transfer.<sup>39</sup> Second, even if the external mass transfer limitation could be eliminated completely, the reduction reaction may also be controlled by the internal mass transfer, as shown in this study. The effectiveness factor for the internal diffusion decreases as the temperature increases, indicating that the reducing gas permeating into the particles becomes more difficult, which results in the decrease of the gas–solid contact surface. The decreased reaction surface partially offsets the reactivity-induced improvement of the overall reaction rate as the temperature, contributing to much lower sensitivity of the apparent reaction rate with the temperature than that of the intrinsic reaction rate, and the apparent activation energy is then smaller than the intrinsic activation energy. Finally, the kinetic compensation effect may also lead to a low activation energy. However, a low pre-exponential factor will certainly be obtained simultaneously, and the two lower values for the parameters make no physical sense. As well known in the quantum chemistry calculation, the reaction rate has a lower sensitivity to the pre-exponential factor than the activation energy. Therefore, to obtain the intrinsic kinetics in the fitting process, the pre-exponential factor should be restricted in the order of magnitude as its physical background. Only in this way, the comparison of the activation energy is meaningful.

Although the intrinsic reduction kinetics of the hematite OC by CO was obtained in this work, the mechanism of the reactions at the molecular level is still unknown. That is to say, the reaction coordinate is still unclear. However, the kinetics is highly dependent upon the reaction mechanism. Although some DFT simulation results have been reported, it is still not so confident to accept these mechanism results as a result of the inherent disadvantage of the simulation and the complexity of the reaction pathway. The aim of this work is to establish the relation between the DFT simulation results and the experimental results; this is only a preliminary step forward obtained now, and more work is required in the future.

Through analysis of the internal and external diffusion factors, it is clear that the overall reaction may be affected by the external mass transfer under a high temperature condition and the reaction process can be described by the shrinking core series model. Further work should be performed with comprehensive consideration of the intrinsic kinetics, reactive surface, and internal/external diffusion to build a CFD-simulation-applicable model. The basic idea is shown in Figure 11. This model will suit not only regime I but also regimes II and III.

## 5. CONCLUSION

In this work, the intrinsic kinetics of the first reduction stage of a hematite OC reduced by CO was carefully investigated.

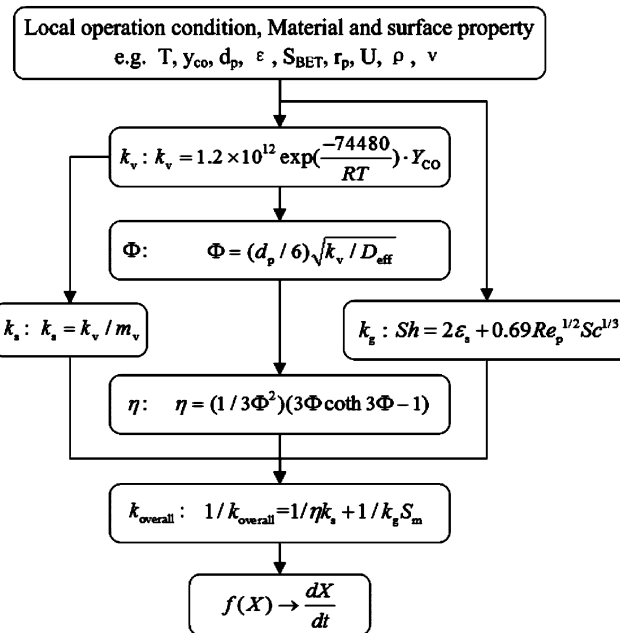


**Figure 11.** From the intrinsic kinetics to the CFD-simulation-applicable model.

Initially, the BET surface area and pore size distribution were obtained to provide fundamental data for the kinetics analysis. After that, temperature-programmed reduction experiments were conducted in TGA. The results showed that the weight loss rate demonstrates a bimodal distribution. For the first reduction stage of this hematite OC, the appropriate experimental temperature range for the intrinsic kinetics testing was determined as 400–650 °C. Additionally, a series of formal experiments were further conducted in a batch fluidized bed rig with different temperatures and different CO concentrations. After elimination of the internal and external diffusion limitations, the intrinsic activation energy and pre-exponential factor were determined as 74.48 kJ/mol and  $1.2 \times 10^{12} \text{ s}^{-1}$ , respectively. The analysis of the internal and external diffusion factors is beneficial to understand the reaction characteristics of this kind of hematite OC. The external diffusion control and the smaller apparent activation energy attained in previous studies can be well-explained by the result obtained in this work. This study can also help to develop the applicable model for CFD simulation.

## AUTHOR INFORMATION

### Corresponding Authors

\*E-mail: sumingze\_reneng@126.com.

\*E-mail: zgliu9322@163.com.

### ORCID ®

Mingze Su: 0000-0001-7828-7468

Haibo Zhao: 0000-0003-4700-4933

### Notes

The authors declare no competing financial interest.

## ACKNOWLEDGMENTS

This work was financially supported by the National Key Special Project (2016YFB0600801), the National Natural Science Foundation of China (51406110), the Foundation for Outstanding Young Scientist in Shandong Province (BS2014NJ013), the Fundamental Research Foundation of

Shandong Academy of Sciences (2015-08), and the Youth Science Fund Project of Shandong Academy of Sciences (2014QN014).

## ■ REFERENCES

- (1) Fan, L. S.; Li, F. *Ind. Eng. Chem. Res.* **2010**, *49*, 10200–10211.
- (2) Zhao, H.; Liu, L.; Wang, B.; Xu, D.; Jiang, L.; Zheng, C. *Energy Fuels* **2008**, *22*, 898–905.
- (3) Knoche, K.; Richter, H. *Brennst.-Waerme-Kraft* **1968**, *20*, 205.
- (4) Richter, H. J.; Knoche, K. F. Reversibility of combustion processes. In *Efficiency and Costing*; Gaggioli, R. A., Ed.; American Chemical Society (ACS): Washington, D.C., 1983; ACS Symposium Series, Vol. 235, Chapter 3, pp 71–85.
- (5) Elgeassy, A.; Shehata, K.; Ezz, S. T. *Iron Steel Inst. Jpn.* **1977**, *17*, 629–635.
- (6) Ettabirou, M.; Dupré, B.; Gleitzer, C. *Steel Res.* **1986**, *57*, 306–311.
- (7) Wang, B.; Lv, H.; Zhao, H.; Zheng, C. *Procedia Eng.* **2011**, *16*, 390–395.
- (8) Zafar, Q.; Mattisson, T.; Gevert, B. *Energy Fuels* **2006**, *20*, 34–44.
- (9) Garcia-Labiano, F.; de Diego, L. F.; Adanez, J.; Abad, A.; Gayan, P. *Ind. Eng. Chem. Res.* **2004**, *43*, 8168–8177.
- (10) Garcia-Labiano, F.; Adanez, J.; de Diego, L. F.; Gayan, P.; Abad, A. *Energy Fuels* **2006**, *20*, 26–33.
- (11) Chen, H.; Zheng, Z.; Shi, W. *Procedia Eng.* **2015**, *102*, 1726–1735.
- (12) Monazam, E. R.; Breault, R. W.; Siriwardane, R.; Richards, G.; Carpenter, S. *Chem. Eng. J.* **2013**, *232*, 478–487.
- (13) Abad, A.; Garcia-Labiano, F.; de Diego, L. F.; Gayan, P.; Adanez, J. *Energy Fuels* **2007**, *21*, 1843–1853.
- (14) Go, K. S.; Son, S. R.; Kim, S. D. *Int. J. Hydrogen Energy* **2008**, *33*, 5986–5995.
- (15) Piotrowski, K.; Mondal, K.; Lorethova, H.; Stonawski, L.; Szymański, T.; Wiltowski, T. *Int. J. Hydrogen Energy* **2005**, *30*, 1543–1554.
- (16) Piotrowski, K.; Mondal, K.; Wiltowski, T.; Dydo, P.; Rizeg, G. *Chem. Eng. J.* **2007**, *131*, 73–82.
- (17) Pineau, A.; Kanari, N.; Gaballah, I. *Thermochim. Acta* **2006**, *447*, 89–100.
- (18) Su, M.; Ma, J.; Tian, X.; Zhao, H. *Fuel Process. Technol.* **2017**, *155*, 160–167.
- (19) Chuang, S. Y.; Dennis, J. S.; Hayhurst, A. N.; Scott, S. A. P. *Proc. Combust. Inst.* **2009**, *32*, 2633–2640.
- (20) Dong, C.; Sheng, S.; Qin, W.; Lu, Q.; Zhao, Y.; Wang, X.; Zhang, J. *Appl. Surf. Sci.* **2011**, *257*, 8647–8652.
- (21) Zhang, X.; Dong, C.; Zhang, J.; Jiang, D.; Yang, Y. The reaction path of CO and Fe<sub>2</sub>O<sub>3</sub> in a chemical-looping combustion system. *Proceedings of the International Conference on Sustainable Power Generation and Supply (SUPERGEN '09)*; Nanjing, China, April 6–7, 2009.
- (22) Dong, C.; Liu, X.; Qin, W.; Lu, Q.; Wang, X.; Shi, S.; Yang, Y. *Appl. Surf. Sci.* **2012**, *258*, 2562–2569.
- (23) Tan, Q.; Qin, W.; Chen, Q.; Dong, C.; Li, W.; Yang, Y. *Appl. Surf. Sci.* **2012**, *258*, 10022–10027.
- (24) Qin, W.; Chen, Q.; Wang, Y.; Dong, C.; Zhang, J.; Li, W.; Yang, Y. *Appl. Surf. Sci.* **2013**, *266*, 350–354.
- (25) Qin, W.; Wang, Y.; Dong, C.; Zhang, J.; Chen, Q.; Yang, Y. *Appl. Surf. Sci.* **2013**, *282*, 718–723.
- (26) Ma, J.; Zhao, H.; Tian, X.; Wei, Y.; Rajendran, S.; Zhang, Y.; Bhattacharya, S.; Zheng, C. *Appl. Energy* **2015**, *157*, 304–313.
- (27) Ma, J.; Zhao, H.; Tian, X.; Wei, Y.; Zhang, Y.; Zheng, C. *Energy Fuels* **2015**, *29*, 3257–3267.
- (28) Su, M.; Zhao, H.; Ma, J. *Energy Convers. Manage.* **2015**, *105*, 1–12.
- (29) Wen, C. Y.; Yu, Y. H. *AIChE J.* **1966**, *12* (3), 610–612.
- (30) Breault, R. W.; Yarrington, C. S.; Weber, J. M. *J. Energy Resour. Technol.* **2016**, *138*, 042202.
- (31) Monson, C. R.; Germane, G. J.; Blackham, A. U.; Smoot, L. D. *Combust. Flame* **1995**, *100* (4), 669–683.
- (32) Fogler, H. S. *Elements of Chemical Reaction Engineering*; Prentice Hall: Upper Saddle River, NJ, 1992; pp 2493.
- (33) Breault, R. W. *Powder Technol.* **2006**, *163*, 9–17.
- (34) Abad, A.; Adánez, J.; García-Labiano, F.; de Diego, L. F.; Gayán, P. *Combust. Flame* **2010**, *157*, 602–615.
- (35) Xiao, R.; Song, Q. *Combust. Flame* **2011**, *158* (12), 2524–2539.
- (36) Thiele, E. W. *Ind. Eng. Chem.* **1939**, *31*, 916–920.
- (37) Wakao, N.; Smith, J. M. *Chem. Eng. Sci.* **1962**, *17*, 825–834.
- (38) Monazam, E. R.; Breault, R. W.; Siriwardane, R. *Chem. Eng. J.* **2014**, *242* (242), 204–210.
- (39) Sun, K. *Macroscopic Reaction Kinetics and Its Analytical Method*; Metallurgy Industry Press: Beijing, China, 1998; pp 4.